Physics of Fluids

Vacuum suction unit based on the zero pressure difference method

Cite as: Phys. Fluids **32**, 017104 (2020); https://doi.org/10.1063/1.5129958
Submitted: 04 October 2019 . Accepted: 23 November 2019 . Published Online: 14 January 2020

Kaige Shi (施凯戈), and Xin Li (黎鑫)

COLLECTIONS

F This paper was selected as Featured

ARTICLES YOU MAY BE INTERESTED IN

Vacuum suction unit based on the zero pressure difference method

Cite as: Phys. Fluids 32, 017104 (2020); doi: 10.1063/1.5129958
Submitted: 4 October 2019 • Accepted: 23 November 2019 •
Published Online: 14 January 2020

Kaige Shi (施凯戈) and Xin Li (黎鑫)[a)]

AFFILIATIONS

The State Key Laboratory of Fluid Power and Mechatronic Systems, Zhejiang University, Hangzhou 310027, China

[a)]**Email:** vortexdoctor@zju.edu.cn

ABSTRACT

Vacuum suction units are widely used in various manufacturing lines, climbing robots, etc. Their most difficult problem is vacuum leakage, which leads to suction failure. Vacuum leakage is traditionally prevented by blocking the flow path between the atmosphere and the vacuum zone, which is difficult for a suction unit working on a rough surface. This paper proposes using the zero pressure difference (ZPD) method, which is based on a completely different mechanism. The ZPD method eliminates the pressure difference at the boundary of the vacuum zone, so vacuum leakage can be prevented regardless of the roughness of the working surface. A new vacuum suction unit based on the ZPD method was designed, fabricated, and tested. The ZPD suction unit forms a rotating water layer on the periphery of the vacuum zone, and the resulting inertial force generates a steep pressure gradient so that a high vacuum is maintained at the center of the vacuum zone while the pressure at the boundary remains equal to the atmospheric pressure. Experiments showed that a 0.8-kg ZPD suction unit generated a suction force of over 245 N on rough surfaces with a power consumption of less than 400 W. In contrast, a traditional suction unit of the same size would need a vacuum pump consuming several kilowatts and weighing dozens of kilograms to generate a similar suction force because of severe vacuum leakage. The ZPD suction unit was then successfully applied to a robotic arm, wall-climbing robot, and spider-man wall-climbing device.

I. INTRODUCTION

The tremendous suction force caused by a vacuum was first demonstrated by Otto von Guericke in 1654 via his famous Magdeburg hemisphere experiment, in which teams of horses failed to separate two hemispheres from which the air had been partially evacuated. Compared with other adhesion methods (e.g., magnetic adhesion,[1–3] electrostatic adhesion,[4–6] and bioinspired adhesion[7–13]), vacuum suction can generate a stable suction force regardless of the substrate material with easy engagement and disengagement. Therefore, vacuum suction units are widely used as manipulators to grip and handle a variety of objects in industry,[14–18] agriculture,[19–21] surgery,[22–24] and other fields. They are also applied in numerous wall-climbing robots with different functions (e.g., cleaning the glass walls of high-rise buildings[25–27] and inspecting hostile constructions[28–30]).

However, the application of a vacuum suction unit is greatly constrained by vacuum leakage. Figure 1 shows a schematic of a vacuum zone in the atmosphere. Vacuum leakage is the air flow from the atmosphere to the vacuum zone driven by the pressure difference at the boundary of the vacuum zone (shown by a broken line). There are two necessary conditions for vacuum leakage: a flow path connecting the atmosphere and vacuum zone and a pressure difference at the boundary of the vacuum zone.

Vacuum leakage is traditionally prevented by blocking the flow path at the boundary (i.e., breaking the first condition for vacuum leakage). Figure 2(a) shows a traditional vacuum suction unit with a cylindrical chamber. There is a soft sealing ring on the periphery of the chamber, and the chamber in the center is connected to a vacuum source (e.g., vacuum pump or vacuum ejector[31,32]). For operation on a smooth surface, the sealing ring is pressed against the surface to completely block the flow path between the vacuum zone and the atmosphere. As the initial air in the chamber is evacuated by a vacuum pump, a vacuum zone is created in the chamber. The pressure distribution on the working surface is plotted in Fig. 2(a) (the experimental method and setup are described in Appendix A). As indicated by the red circles, the pressure in the chamber is uniform and 90 kPa below atmospheric pressure [i.e., −90 kPa (g)].

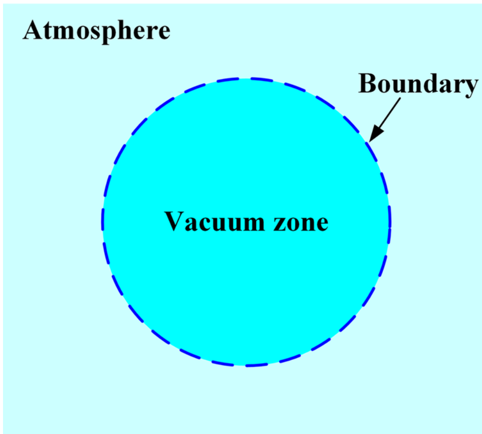

FIG. 1. Schematic of vacuum leakage.

In this case, vacuum leakage does not occur because there is no flow path from the vacuum zone to the atmosphere. However, when the working surface is rough, although the soft sealing ring can deform to a certain extent to tightly contact the surface, gaps form between the sealing ring and the rough surface. This creates flow paths that connect the vacuum zone and atmosphere [see Fig. 2(b)]. In this case, because both conditions are satisfied, vacuum leakage occurs. The leakage air flows through the gaps and forms a gradually changing pressure distribution in the sealing ring; it then flows into the chamber and breaks the pressure state of the vacuum zone. Figure 2(b) shows the resulting pressure distributions on sandpaper with roughnesses of P120 and P60, respectively. As the working surface becomes rougher, the gaps get larger, and the flow resistance of the gaps becomes smaller. Consequently, the flow rate of the vacuum leakage increases, which eventually causes the vacuum zone in the chamber to vanish.

The traditional method of blocking the flow path fails to prevent vacuum leakage on rough and uneven surfaces. Some researchers have improved the structure of the sealing ring to increase the flow resistance. For example, Zhao *et al.* proposed a sealing mechanism with an air spring and regulating springs.[33] Longo and Muscato designed a sandwich of Teflon/bristle sealing for the vacuum suction unit of their wall-climbing robot.[34] Koo *et al.* installed a double-layer rubber ring consisting of a flexible bending layer and a single straight layer on their vacuum suction unit.[35] Nevertheless, all of these improvements are within the scope of the traditional method. Thus, none of them can effectively avoid vacuum leakage and maintain the vacuum state on rough and uneven surfaces.

In this article, we propose a new method to prevent vacuum leakage that eliminates the pressure difference at the boundary of the vacuum zone (i.e., breaking the second condition of vacuum leakage), which we call the zero pressure difference (ZPD) method.

II. ZERO PRESSURE DIFFERENCE METHOD

A. Mechanism

In order to eliminate the pressure difference at the boundary of the vacuum zone, the pressure at the boundary must be equal to the atmospheric pressure, while a high vacuum is maintained in the zone. Therefore, a stable pressure gradient must be established near the boundary. As shown in Fig. 3, the ZPD method builds a rotating water layer on the periphery of the vacuum zone to create a sharp pressure gradient. The pressure inside the water layer is a high vacuum. The pressure increases in the radial direction and reaches atmospheric pressure outside the water layer (i.e., boundary of the vacuum zone). There is no pressure difference at the boundary of the vacuum zone, so the second condition for vacuum leakage is broken.

Figure 4 is a schematic of a new vacuum suction unit based on the ZPD method (i.e., ZPD suction unit). A fan is set in the chamber and fixed on the motor shaft. As shown in Fig. 4, the outer radius of the fan R_f is slightly smaller than R to avoid scratch, so the fan region is within and slightly smaller than the vacuum chamber. Water is injected into the chamber. When the ZPD suction unit is operating, the fan rotates to drive the water and air in the chamber to rotate. Because water is denser than air, it accumulates on the periphery,

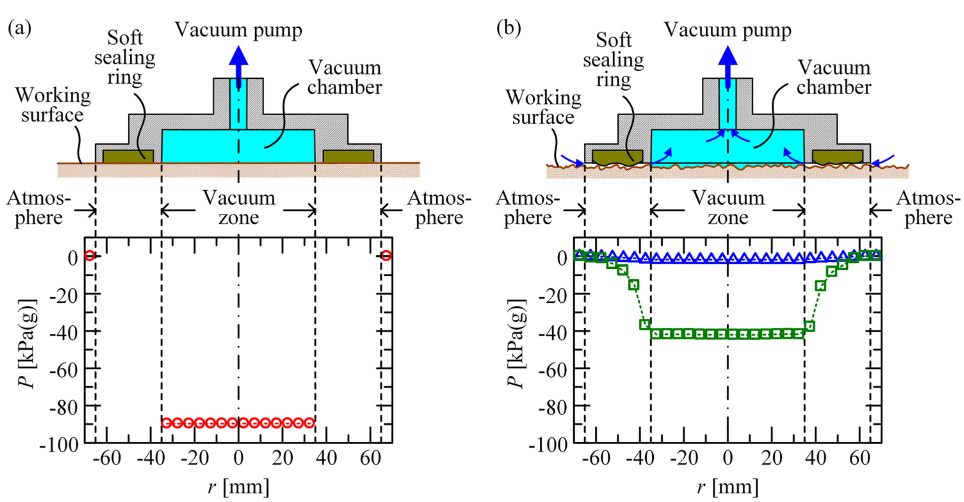

FIG. 2. Traditional vacuum suction unit. (a) Traditional suction unit on a smooth surface. The red circles indicate the experimental pressure distribution on the smooth surface. (b) Traditional suction unit on rough surfaces. The blue triangles and green squares indicate pressure distributions on P120 and P60 sandpaper, respectively.

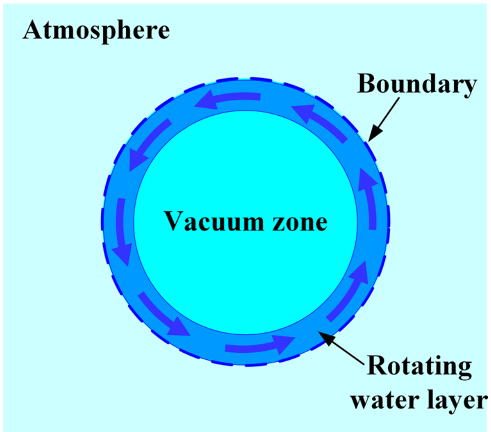

FIG. 3. Schematic of the ZPD method.

while the air occupies the center of the chamber. If the fluid in the chamber is assumed to be fully driven by the fan, the fluid rotates at the same rotational speed ω as the fan, which means that the tangential velocity u_α of the fluid is equal to ωr (where r is the radius position). The rotating flow and its resulting inertial effect $\rho {u_\alpha}^2/r$ are dominant, while the effect of other velocity components and the viscous effect are small in comparison and thus can be neglected. The motion equation of the fluid (i.e., Navier–Stokes equation) in the chamber can be simplified as

$$\rho\omega^2 r = \frac{\partial P}{\partial r}. \tag{1}$$

Substituting the density of air ρ_a and density of water ρ_w into ρ in (1) and integrating (1) in r lead to the following pressure distribution in the chamber:

$$P(r) = \begin{cases} \frac{1}{2}\rho_a\omega^2 r^2 + P_c (0 \le r \le R - \delta), \\ \frac{1}{2}\rho_w\omega^2\left(r^2 - R^2\right) + P_b (R - \delta < r \le R), \end{cases} \tag{2}$$

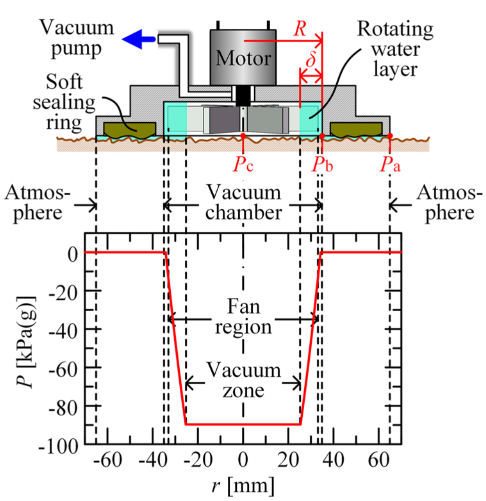

FIG. 4. Schematic of the ZPD suction unit. The red line indicates the pressure distribution based on (2) for ω = 93.4 rps and δ = 9 mm.

where R is the radius of the vacuum chamber, δ is the thickness of the water layer, and P_c and P_b are the pressures at $r = 0$ and $r = R$, respectively. As an example, if the rotation speed ω of the fan is 93.4 rps and the water layer thickness δ is 9 mm, the pressure distribution $P(r)$ that forms in the chamber is as shown in Fig. 4. The following can be observed:

(1) A sharp and quadratic pressure distribution is formed within the rotating water layer because of the high density of water. The pressure difference on either side of the 9 mm thick water layer can be as high as 90 kPa [i.e., outside the water layer is 0 kPa (g) while inside is −90 kPa (g)].
(2) A pressure gradient also forms in the center but is tiny because air is much less dense than water. According to Li's group,[36–38] the pressure difference generated by a rotating air flow is usually within hundreds of pascals. In addition, the high vacuum in the center further reduces ρ_a and the pressure gradient. Therefore, the pressure in the center can be considered uniform [i.e., $P(r) = P_c$, where $r < R - \delta$].
(3) If the pressure gradient at the center is neglected, the continuity of $P(r)$ at $r = R - \delta$ gives (3). This equation implies that P_b can be set to atmospheric pressure by adjusting P_c, ω, and δ such that the pressure difference at the boundary of the vacuum zone can be eliminated. As a result, the vacuum leakage can be prevented even on rough and uneven surfaces,

$$P_b = P_c + \tfrac{1}{2}\rho_w\omega^2\left(2R\delta - \delta^2\right). \tag{3}$$

As shown in Fig. 4, the air-water interface is usually located in the fan region, which means the vacuum zone is smaller than the fan region.

B. Design of a prototype

To implement the new method, we needed to design a ZPD suction unit. The key to the design was to make the target variable P_b equal to the atmospheric pressure P_a. We adopted the design scheme shown in Fig. 5(a) to supply water to the ZPD suction unit and build a control system for P_b. There is an annular reservoir outside the chamber. The reservoir and chamber are connected by several circumferentially distributed orifices. The water in the reservoir is supplied by an external water source, and a pressure regulator is used to make the pressure in the reservoir P_r equal to atmospheric pressure. When the vacuum inside the chamber pressure zone boundary deviates from atmospheric pressure, the thickness of the water layer can be adjusted automatically. For example, at a given pressure of the vacuum pump P_c and rotational speed ω, when $P_b < P_a$, the pressure difference ΔP drives the water flow from the reservoir to the chamber through the orifices to increase the thickness of the water layer and thus P_b. When $P_b > P_a$, the water in the chamber flows to the reservoir, which decreases the thickness of the water layer and thus P_b. This process can be described by the control block diagram in Fig. 5(b); P_r is the system input (=P_a), and the boundary pressure P_b is the output. This is a closed-loop control system with an integral, so the output of the system can be automatically adjusted to the input, even when the pressure of the vacuum pump P_c and rotation speed ω change. In addition, if there is a gap between the soft sealing ring and the surface, a small amount of water leaks because of the effect of gravity at a flow rate of q_{leak}. Because the leakage flow is

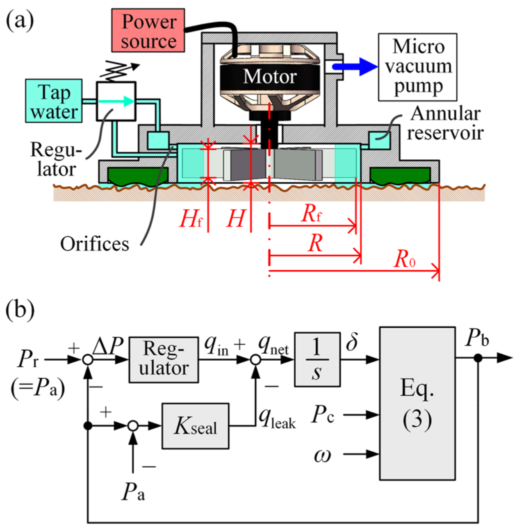

FIG. 5. Mechanism of the ZPD suction unit. (a) Schematic. (b) Pressure control system.

generally viscous, q_{leak} is proportional to the difference between P_b and P_a with the coefficient being a constant K_{seal}. The effect of q_{leak} can also be compensated for by the closed-loop control system in Fig. 5(b). A detailed analysis of the system in Fig. 5(b) is provided in Appendix B.

Figure 6(a) shows the structure of the ZPD suction unit. The inlet of the regulator is connected to a water tap, while the outlet is connected to the annular reservoir. The regulator and ZPD suction unit are integrated and 3D printed. Similar to traditional vacuum suction units, a nitrile foam rubber ring is embedded on the periphery of the chamber. The motor that drives the fan is fixed in the motor chamber with its shaft extending to the chamber through a hole that connects the chamber of the vacuum zone with the motor chamber. A micro-vacuum pump is used to evacuate the initial air and create a vacuum zone in the chamber. Figure 6(b) is a photograph of the ZPD suction unit, and its dimensions are listed in Table I.

TABLE I. Geometric parameters of the ZPD suction unit.

R_0 (mm)	R (mm)	H (mm)	R_f (mm)	H_f (mm)
65	35	14	33	10

III. RESULTS AND DISCUSSIONS

A. Experimental verification

1. Static characteristics

The pressure distributions of the ZPD suction unit on three surfaces (i.e., smooth acryl and P120 and P60 sandpapers) were measured using the experimental setup introduced in Appendix A 1, and the results have been plotted in Fig. 7. The experimental results (points in the figure) clearly show that a flat pressure distribution formed at the center of the vacuum zone, while a pressure gradient gradually rising to atmospheric pressure formed at the periphery

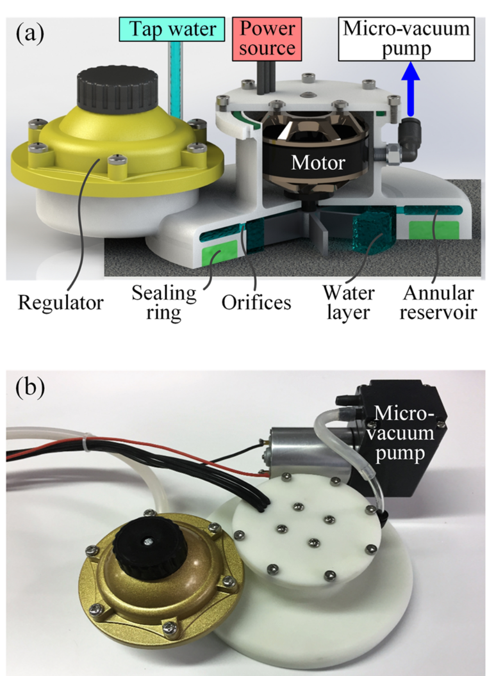

FIG. 6. Rendering and photograph of the ZPD suction unit. (a) Rendering. (b) Photograph.

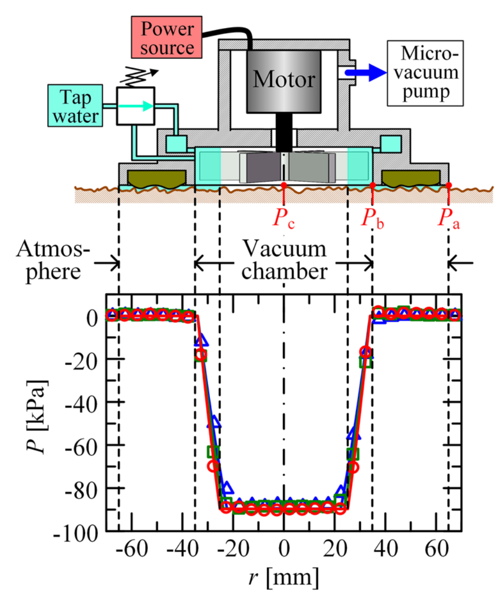

FIG. 7. Pressure distributions of the prototype on various surfaces. The red circles, green squares, and blue triangles represent experimental pressure distributions on a smooth acryl surface and P120 and P60 sandpaper, respectively. The red, green, and blue lines represent the theoretical pressure distributions on a smooth acryl surface and P120 and P60 sandpaper, respectively.

of the vacuum zone (i.e., within the rotating water layer). The negative pressure in the vacuum zone was clearly unaffected by the surface roughness. Although the rough surface of the sandpaper created gaps, vacuum leakage did not occur because of the atmospheric pressure at the boundary of the vacuum zone.

We recorded the motor speed for the smooth surface and P120 and P60 sandpaper: ω = 93.4, 88.0, and 83.3 rps, respectively. As the surface roughness increased, so did the resistance to the fan rotating the water layer. Thus, the rotational speed of the fan decreased slightly. Substituting the measured values of the rotational speed ω, central pressure P_c and boundary pressure P_b into (2) gave the theoretical pressure distribution, which is shown by the solid lines in Fig. 7. The theoretical curves agreed well with the experimental data. The zone with the pressure gradient indicates the thickness of the water layer. For the smooth surface, the water layer was 10 mm thick. With rougher surfaces, the thickness of the water layer increased to 11 and 13 mm. This is because a decreasing rotational speed required a thicker water layer to overcome the pressure difference between the atmosphere and the vacuum zone. Figure 8 shows the suction value F_s measured on five surfaces at a constant rotational speed of 90 rps: smooth surface, P120 sandpaper, P60 sandpaper, tiled wall, and concrete floor with rocks. The experimental values of F_s were measured using the setup in Appendix A 2. The different working surfaces only caused a 2% difference in the suction force; in other words, F_s was almost constant regardless of the working surface. This result proves that the ZPD method can effectively prevent vacuum leakage.

2. Dynamic response

Supplementary material, Video 1 and Fig. 9(c) record a working cycle of the ZPD suction unit. The ZPD suction unit was fixed vertically, and a transparent acryl disc was used as the working surface [see Figs. 9(a) and 9(b)]. In order to simulate the leakage path, eight radial grooves that were 10 mm wide and 2 mm deep were made on the periphery of the acryl disc. At t = 0, the ZPD suction unit began to work. The water was ejected into the chamber and rotated by the fan to form a rotating water layer. After about 4 s, the flow in the ZPD suction unit became stable. The rotational speed ω was controlled to 70 rps, and P_c of the vacuum zone reached the minimum pressure (−90 kPa) of the micro-vacuum pump. Although the water in the chamber kept leaking through the radial grooves on the workpiece at a leakage flow rate q_{leak} of about 0.5 l/min, the rotating water layer and vacuum state in the vacuum zone were maintained well.

Next, we experimentally investigated the response of the ZPD suction unit when we changed the water leakage, pressure of vacuum zone, and rotational speed.

(1) At about t = 10 s, an additional flow path connecting the chamber to the atmosphere (see Fig. 9) was opened by an on–off valve, and an additional water leakage was suddenly created. As a result, q_{leak} increased to around 0.8 l/min. The additional water leakage was immediately compensated for by the regulator. Thus, the sudden change in q_{leak} had no effect on the rotating water layer and pressure state of the vacuum zone.

(2) At about t = 25 s, P_c was deliberately changed from −90 kPa to −40 kPa by adjustment of the power of the micro-vacuum pump. The sudden rise in P_c increased P_b, as can be predicted by (3). The increase in P_b reduced the inlet water flow rate q_{in}, which reduced δ. As the thickness of the water layer decreased, P_b returned to P_r. Conversely, at t = 33 s, P_c came back to −90 kPa; P_b stayed below P_r for about 1 s, during which q_{in} increased. This increased δ and brought P_b back to P_r.

(3) At about t = 41 s, the rotational speed ω was deliberately increased to 100 rps. According to the control block diagram in Fig. 5(b), P_b increased immediately, and q_{in} decreased. Consequently, the thickness of the water layer decreased, and P_b dropped back to P_r. At t = 49 s, ω was reduced to 70 rps. As predicted, P_b decreased, which increased q_{in}. Thus, the thickness of the water layer increased, and P_b rose to P_r.

The above process verifies the block diagram in Fig. 5(b) and indicates that the ZPD suction unit with negative feedback can operate stably regardless of changes in q_{leak}, P_c, and ω. Furthermore, we found that the dynamic responses of the ZPD suction unit on rough surfaces are similar to that in Fig. 9(c). This is because the additional resisting torque and the additional water leakage caused by the roughness of the working surface can be compensated

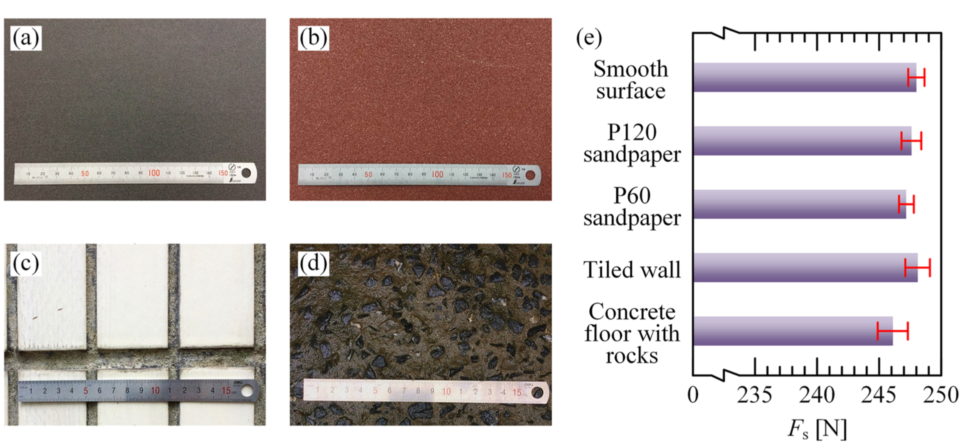

FIG. 8. Suction force on various surfaces. (a) Photograph of the P120 sandpaper. (b) Photograph of the P60 sandpaper. (c) Photograph of the tiled wall. (d) Photograph of the concrete floor with rocks. (e) Suction force on various surfaces.

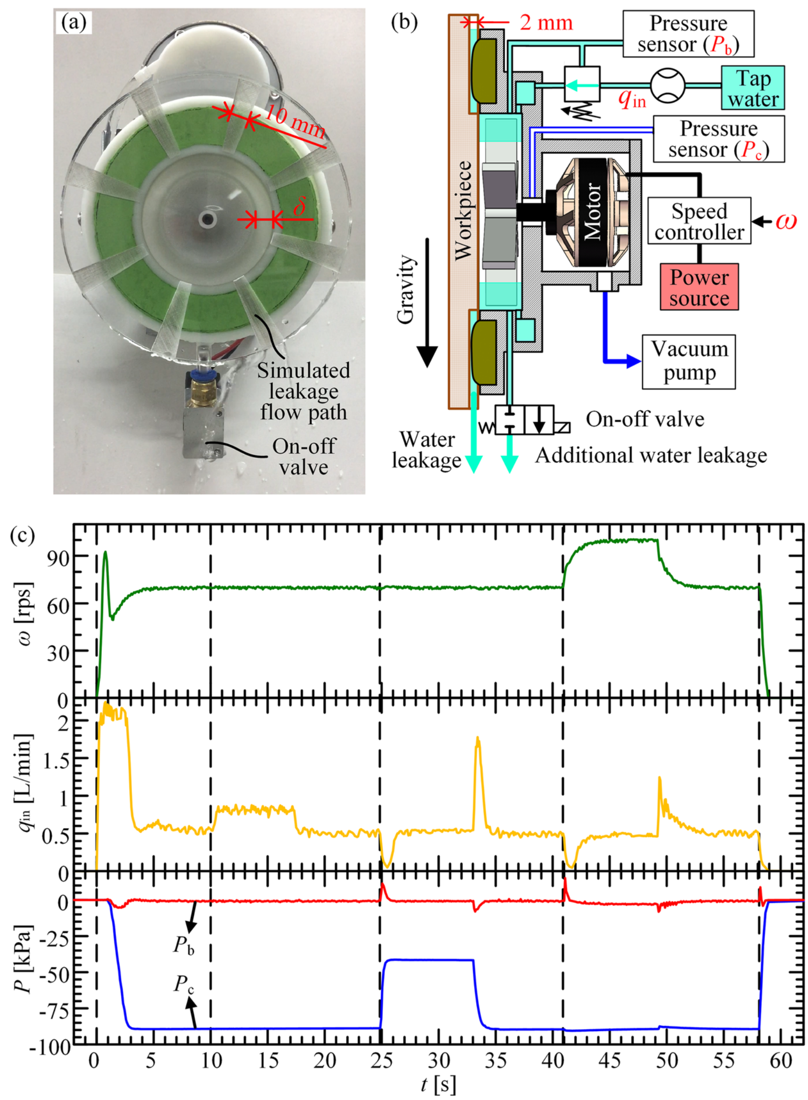

FIG. 9. Experimental setup and results for dynamic testing of the ZPD suction unit. (a) Image of the setup. (b) Schematic of the setup. A flowmeter is used to detect the inlet water flow rate q_{in}. The water in the vacuum chamber leaks through either the radial grooves or the additional flow path controlled by the on–off valve. The power of the vacuum pump can be adjusted, so P_c can be changed. The speed controller can control the rotating speed to the demanded value. The transient rotating speed can be read from the speed controller. (c) Experimental results.

by the rotating speed controller and the water pressure regulator, respectively.

B. Power consumption

Figure 10 plots the power consumption of the ZPD suction unit on various surfaces under the conditions of ω = 90 rps and P_c = −90 kPa. The power comprised two components: the power of the vacuum pump and the power of the motor driving the fan.

The ZPD method ensures no pressure difference and no vacuum leakage on the boundary of the vacuum zone on any surface. The vacuum pump evacuates the initial air from the chamber when the prototype started. While the ZPD suction unit is operating, the vacuum pump has its lowest power consumption with a zero intake flow rate. Therefore, the power of the vacuum pump can be very low. We adopted a micro-vacuum pump for the ZPD suction unit with a rated power and weight of only 10 W and 270 g, respectively. Moreover, the power of the vacuum pump does not change with the surface roughness.

Compared with the low power consumption of the micro-vacuum pump, the power of the motor reaches hundreds of watts and increases with the roughness of the working surface. The small power consumption of the pump and the large power consumption of the motor are both owing to the natural characteristics of the ZPD suction unit. The motor has to overcome the frictional resistance torque between the fluids (i.e., the rotating water layer and air in the chamber) and wall (i.e., the inner surfaces of the chamber and working surface). Because air is much less dense and viscous than water, especially in a high vacuum, we only need to consider the resistance torque generated by the rotating water layer. The resistance torques on the upper surface of the chamber, cylindrical surface of the chamber, and working surface are represented by T_{upp}, T_{cyl}, and T_{wor}, respectively, and are expressed below. A detailed derivation based on empirical wall functions[39,40] is presented in Appendix C,

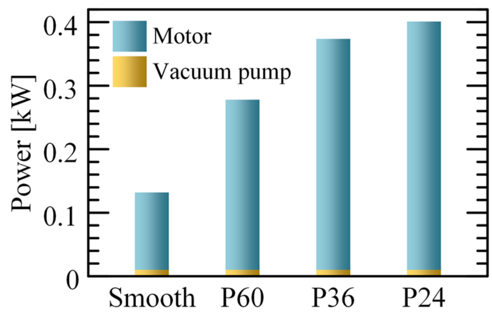

FIG. 10. Power consumption of the prototype on various surfaces.

$$T_{upp} = \frac{0.18\pi\rho^{\frac{3}{4}}\mu^{\frac{1}{4}}\omega^{\frac{7}{4}}\left[R^{\frac{19}{4}} - (R-\delta)^{\frac{19}{4}}\right]}{19\left(\frac{H-H_f}{2}\right)^{\frac{1}{4}}}, \tag{4}$$

$$T_{cyl} = \frac{0.045\pi\rho^{\frac{3}{4}}\mu^{\frac{1}{4}}\omega^{\frac{7}{4}}R_f^{\frac{7}{4}}R^2H}{(R-R_f)^{\frac{1}{4}}}, \tag{5}$$

$$T_{wor} = \begin{cases} \dfrac{0.18\pi\rho^{\frac{3}{4}}\mu^{\frac{1}{4}}\omega^{\frac{7}{4}}\left[R^{\frac{19}{4}} - (R-\delta)^{\frac{19}{4}}\right]}{19\left(\frac{H-H_f}{2}\right)^{\frac{1}{4}}}, & \text{smooth,} \\ \dfrac{0.4\pi\rho\omega^2\left[R^5 - (R-\delta)^5\right]}{\left(\frac{1}{0.41}\ln\frac{H-H_f}{2\varepsilon} + 8.5\right)^2}, & \text{rough.} \end{cases} \tag{6}$$

When the rotational speed ω and vacuum pressure P_c are known, we can use (3) to calculate the thickness δ. Then, we can substitute δ into (4)–(6) to calculate the three resistance torques. Finally, the total resistance torque T_{tot} and rotational speed of the water layer ω can be multiplied to obtain the theoretical power consumption of the motor. The calculated power consumptions of the motor on the smooth surface and P60, P36, and P24 sandpaper were 65, 102, 118, and 129 W, respectively. The internal power loss of the motor was not considered in the theoretical calculation, so the values are smaller than those in the experimental results. However, the trend of the theoretical results is consistent with the experimental results. The large power consumption of the motor may be reduced by special treatments of the vacuum chamber wall (e.g., wrinkled surface[41] and superhydrophobic surface[42]), which will be our future research.

C. Comparison of the ZPD and traditional suction units

Experiments were performed to compare the ZPD suction unit with a traditional suction unit. The traditional suction unit consisted of a chamber and sealing ring, as shown in Fig. 2, and it was the same size as the prototype of the ZPD suction unit.

First, the traditional suction unit was tested on four surfaces: a smooth surface and P60, P36, and P24 sandpaper. When the vacuum zone in the chamber was maintained at −80 kPa, vacuum leakage occurred with a rough working surface. A flow rate sensor was installed in the suction port of the vacuum pump to measure the vacuum leakage flow rate. The results are shown in Fig. 11(a). The sealing ring is fit closely on the smooth surface, which resulted in no leakage flow. However, as the surface roughness increased, the leakage flow rate increased dramatically. The air flowing into the chamber expanded rapidly in the very high vacuum. For example, an air flow of 10 l/min at standard pressure [0 kPa (g)] expanded to 50 l/min at −80 kPa (g) vacuum. Therefore, the vacuum pump needed to be very powerful, which would greatly increase the power consumption, weight, and size.

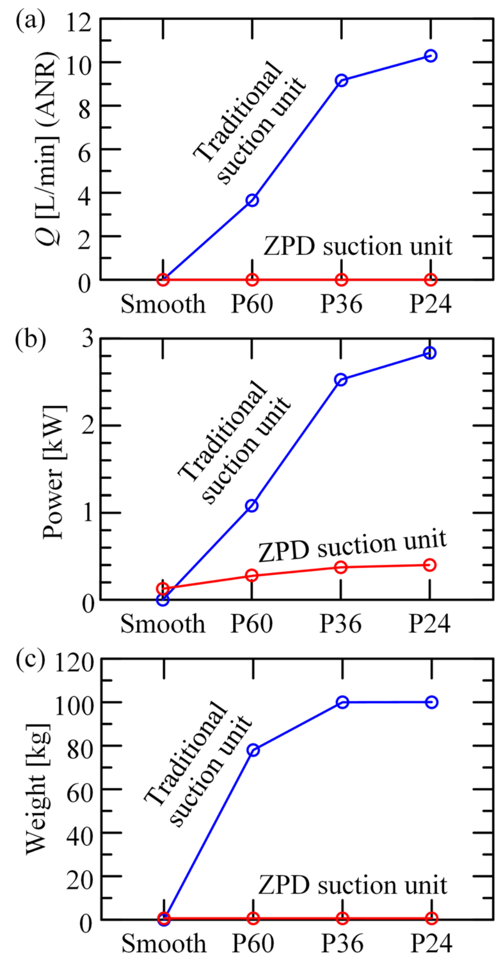

FIG. 11. Comparison of the ZPD and traditional suction units. (a) Leakage flow rate. (b) Total power. (c) Weight.

Two vacuum pumps from Schmaltz Co. (EVE-TR-X 80 AC3 IE3-TYP1 and EVE-TR-X 100 AC3 IE3-TYP1 F) were used to generate vacuum for the traditional suction unit in the experiments. The intake flow rates of the two vacuum pumps at an entrance pressure of −80 kPa were 7.4 and 10.9 l/min (standard reference atmospheric condition, hereafter ANR), respectively. When the leakage flow was 0–7.4 l/min (ANR), the EVE-TR-X 80 AC3 IE3-TYP1 vacuum pump was used, which had a rated power and weight of 2.2 kW and 78 kg, respectively. When the leakage flow was 7.4–10.9 l/min, the EVE-TR-X 100 AC3 IE3-TYP1 F vacuum pump was used, which had a rated power and weight of 3 kW and 100 kg, respectively. Under the assumption that the leakage flow rate is proportional to the power of the vacuum pump, Fig. 11(b) plots the power consumption of the traditional suction unit on the four

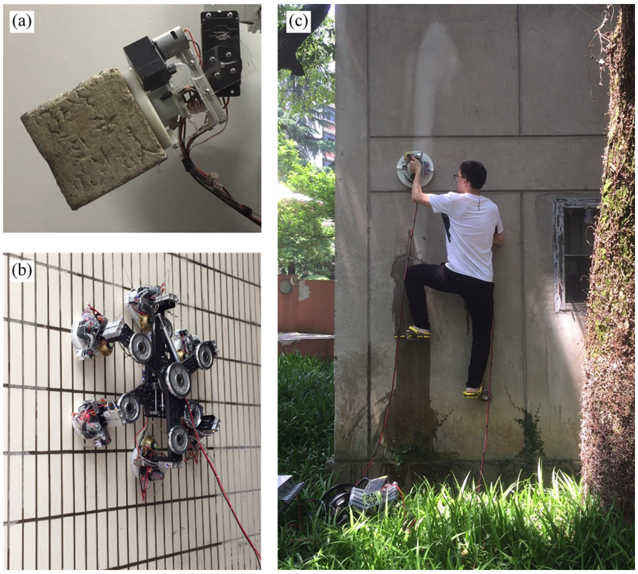

FIG. 12. Applications of ZPD suction units. (a) ZPD suction unit as the end-effector of a robotic arm. (b) ZPD suction units in a hexapod wall-climbing robot. (c) ZPD suction units for a spider-man wall-climbing device.

surfaces: 0, 1.1, 2.5, and 2.8 kW. Figure 11(c) plots the total weight of the traditional suction unit and vacuum pump. The red circles in Fig. 11 indicate the data of the ZPD suction unit. The ZPD suction unit was clearly much more efficient for rough surfaces in terms of the power consumption and weight.

IV. APPLICATIONS

To highlight the versatility of the ZPD suction unit, we present three potential applications in supplementary material, Videos 2–5.

In the first application [Fig. 12(a) and supplementary material, Video 2], the ZPD suction unit (see Table II) was fixed to the end of a robotic arm as a manipulator to grip and handle objects. The rotational speed ω was controlled to 90 rps, and the resulting suction force was 267 N. Therefore, the 10 kg concrete block was easily lifted by the robotic arm and handled with arbitrary poses. The rough surface of the concrete block created flow paths between the atmosphere and the vacuum chamber, so water droplets fell continuously when the ZPD suction unit was placed vertically because of the effect of gravity. However, because of no vacuum leakage, a 10 W micro-vacuum pump was sufficient. If the power for rotating the water layer is considered, the total power consumption of the prototype is only 190 W. In comparison, a traditional suction unit would require a very powerful and heavy vacuum pump to maintain a high vacuum against leakage.

Spenko *et al.* have presented a biologically inspired hexapedal robot that is capable of locomotion on both the ground and a variety of vertical building surfaces.[43] We applied the ZPD suction units to a hexapod robot so that it can climb rough and uneven walls. As shown in Fig. 12(b) and supplementary material Video 3, a robot weighing 16.5 kg maneuvered robustly on a tiled wall [see Fig. 8(c)] with an 11.5 kg payload. The robot was continuously supplied by electrical power and water via a cable and tube. The robot had a ZPD suction unit on each foot; the dimensions are listed in Table II. A single suction unit generated a suction force of about 500 N on the tiled wall, and the measured maximum friction force between the suction unit and the tiled wall was approximately 200 N. Because at least three of its feet were anchored on the wall, the maximum payload of the robot was about 43.5 kg.

Hawkes *et al.* developed a gecko-inspired synthetic adhesion device that enabled a human to climb vertical glass.[44] We applied the ZPD suction unit to a spider-man wall-climbing device. The ZPD suction unit used for this application was the largest in size (see Table II) and generated a suction force of about 2000 N. If the friction coefficient (0.4 on the tiled wall and 0.6 on the concrete wall) is substituted into the Coulomb friction model, the maximum friction force was over 800 N on the tiled wall and 1200 N on the concrete wall, which is more than the weight of an ordinary adult. Therefore, a pair of ZPD suction units can be used in a device for a person to climb vertical walls. As shown in Fig. 12(c) and supplementary material, Videos 4 and 5, a man weighing 67.5 kg climbed the walls with the help of the spider-man wall-climbing device.

TABLE II. Performance of ZPD suction units with various size.

Applications		Robotic arm	Hexapod wall-climbing robot	Spider-man wall-climbing device
Geometry of ZPD suction units	R_0 (mm)	65	80	140
	R (mm)	35	50	100
	H (mm)	14	15	25
	$\mathrm{R_f}$ (mm)	33	48	98
	H_f (mm)	10	10	20
Performance of ZPD suction units	F_s (N)	267 (n = 90 rps)	494 (n = 55 rps)	2005 (n = 28 rps)
	Total power (W)	190 (on concrete surface)	232 (on tiled wall)	658 (on tiled wall)
	Weight (kg)	0.8	1.2	3.0
	Efficiency (N/W)	1.41	2.13	3.05
	Weight-specific suction force (—)	34.1	42.0	68.2
	q_{leak} (l/min)	0.19	1.12	2.11

Table II lists the total power consumptions and weights of the single suction units in the three applications. The efficiency (i.e., ratio between the generated suction force and the consumed electrical power) and weight-specific suction force (i.e., ratio between the generated suction force and the weight of the suction unit) were calculated. Both indices increased significantly with the size of the suction unit. This implies that a suction unit based on the ZPD method can provide better performance for applications that require a large load capacity.

The water leakage flow rates for various suction units are also listed in Table II. Because P_b is usually only slightly higher than P_a, the water leakage flow rate of a ZPD suction unit is small comparing to the air leakage rate of a traditional suction unit for the same rough surface. However, q_{leak} is also affected by the sealing effect between the suction unit and the working surface. When the suction unit for the robotic arm worked on the concrete surface, the steady-state q_{leak} (0.19 l/min) was much smaller than that in Fig. 9 (around 0.5 l/min). This is because the grooves on the working surface greatly affected the sealing effect of the soft sealing ring and caused significant water leakage. Furthermore, q_{leak} of the suction units for the hexapod wall-climbing robot and the spider-man wall-climbing device grew dramatically, which is mainly due to the following two reasons: (1) the grooves between the tiles on the tiled wall, as well as other unevenness of the surface, made the sealing effect poor and (2) the circumference of the vacuum chamber increased as the size of the suction unit increased, which significantly increased the water leakage flow rate. By careful design of the sealing structure of the suction unit, the sealing ring can fit better with the working surface so that the sealing effect can be significantly improved and q_{leak} can be largely decreased. This will be our future research.

V. CONCLUSION

The traditional method to prevent vacuum leakage is to block the flow path between the atmosphere and the vacuum zone. This is difficult to achieve when a suction unit is operating on a rough surface. We propose the ZPD method, which uses a different mechanism to prevent vacuum leakage. The ZPD method eliminates the pressure difference between the atmosphere and the vacuum zone.

We successfully designed and fabricated a ZPD suction unit that uses a rotating water layer to generate a steep pressure gradient on the periphery of the vacuum zone, so a high vacuum can be maintained in the center of the vacuum zone while the pressure at the boundary remains atmospheric. There is a closed-loop control system inside the ZPD suction unit, so the pressure at the boundary is unaffected by water leakage and changes in the central pressure and rotational speed.

Experiments were conducted to investigate the energy consumption of the ZPD suction unit. Because there is no vacuum leakage, a 10 W micro-vacuum pump was sufficient to obtain a high vacuum in the vacuum zone. Meanwhile, the motor that drives the rotating water layer in the chamber consumes more power, and the power consumption increases with the roughness of the working surface. A theoretical model was derived to predict the power required to drive the rotating water layer.

The ZPD suction unit was compared with a traditional suction unit in terms of power consumption and weight. The traditional suction unit can work more efficiently on a smooth surface than the ZPD suction unit. However, as the working surface becomes rough, the vacuum leakage flow rate of the traditional suction unit increases dramatically, which dramatically increases the power consumption and weight of the vacuum pump. In this case, the ZPD suction unit shows its advantage of no vacuum leakage. It consumes much less power, and its weight is tiny compared with the heavy vacuum pump required by the traditional suction unit.

Three ZPD suction units of different sizes were applied to a robotic arm, hexapod wall-climbing robot, and spider-man wall-climbing device. The analysis showed that the suction force increases quadratically with the size of the suction unit. Furthermore, the efficiency and weight-specific suction force were found to increase significantly with the size of the suction unit.

The main limitation of the ZPD method is the demand for high-density fluids such as water. Therefore, the ZPD suction unit cannot be applied in situations where water is not available or needs to be avoided.

SUPPLEMENTARY MATERIAL

See the supplementary material for the following videos:

Video 1: Dynamic response of the ZPD suction unit. Video 2: Test of the suction unit as an end-effector of a robotic arm. Video 3: Test of the suction unit in a hexapod wall-climbing robot. Video 4: Test of the suction unit as a spider-man wall-climbing device on a tiled wall. Video 5: Test of the suction unit as a spider-man wall-climbing device on a concrete wall.

ACKNOWLEDGMENTS

This work was supported by the National Natural Science Foundation of China (Grant Nos. U1613203 and 51975514), Shenzhen Science and Technology Plan (No. JCYJ20170816172938761), and the Fundamental Research Funds for the Central Universities (Grant No. 51221004).

APPENDIX A: EXPERIMENTAL SETUPS AND METHODS

1. Pressure distribution measurement

The pressure distributions in Figs. 2 and 7 were measured with the setup shown in Fig. 13(a). There were 28 linearly distributed pressure taps on the working surface. The inner diameter of the pressure taps was 0.5 mm, and the distance between two adjacent taps was 5 mm. Each pressure tap was connected to a pressure sensor (±100 kPa, CFSensor Co., Ltd.), and the signals from the sensors were acquired by an NI 6211 data acquisition system (DAQ) so that the pressures detected by the sensors could be recorded.

2. Suction force measurement

The experimental setup shown in Fig. 13(b) was used to measure the suction force. The test suction unit worked on a fixed horizontal surface, and an upward force was applied on the suction force via a force sensor (SF-500, AIPU Co., Ltd.). The external force raised the suction unit slowly until the suction unit separated from the working surface. The DAQ recorded the readings from the force sensor during this process. The suction force was obtained by subtracting the weight of the suction unit from the maximum force recorded by the DAQ.

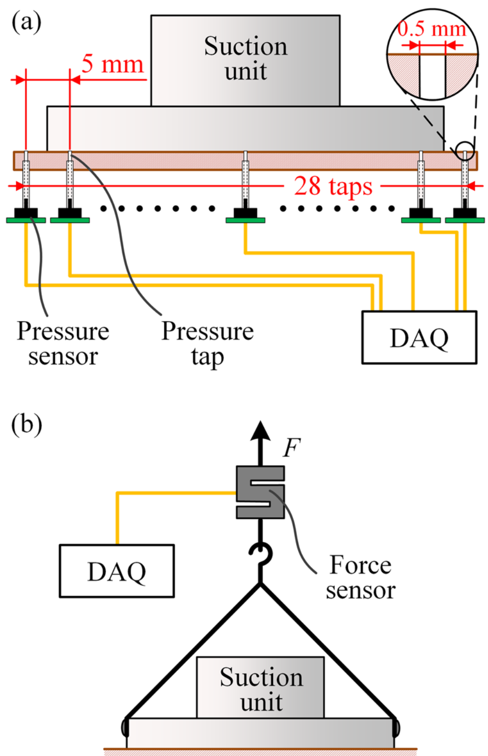

FIG. 13. Schematic of experimental setups. (a) Experimental setup for measuring the pressure distribution. (b) Experimental setup for measuring the suction force.

APPENDIX B: ANALYSIS OF PRESSURE CONTROL SYSTEM

There are some nonlinear elements [i.e., Eq. (3) and the regulator] in the control system in Fig. 5(b), so it is not possible to directly provide the transfer function of the system. In order to obtain the transfer function, the system has to be linearized around a steady state. We use the symbols with overbars (e.g., $\overline{P}_c$, $\bar{\delta}$) to represent the steady-state variables in the steady state. P_b can be expanded into a Tayler series about the steady state as follows:

$$P_b = \overline{P_b} + \frac{\partial P_b}{\partial \delta}\left(\delta - \bar{\delta}\right) + \frac{\partial P_b}{\partial P_c}\left(P_c - \overline{P}_c\right) + \frac{\partial P_b}{\partial \omega}\left(\omega - \bar{\omega}\right) + \cdots \quad \text{(B1)}$$

in which the derivatives are evaluated at the steady state according to (3) as follows:

$$\begin{cases} \frac{\partial P_b}{\partial \delta} = \rho_w \bar{\omega}^2\left(R - \bar{\delta}\right) = K_\delta, \\ \frac{\partial P_b}{\partial P_c} = 1, \\ \frac{\partial P_b}{\partial \omega} = \rho_w \bar{\omega}\left(2R\bar{\delta} - \bar{\delta}^2\right) = K_\omega. \end{cases}$$

Equation (B1) can be rewritten as

$$P_b' = K_\delta \delta' + P_c' + K_\omega \omega', \quad \text{(B2)}$$

where the symbols with an apostrophe are fluctuating parts of the original variables (for example, $\omega' = \omega - \bar{\omega}$). Similarly, the regulator

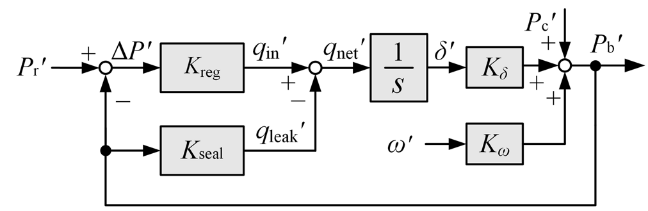

FIG. 14. Linearized pressure control system.

can be linearized as

$$q_{in}' = \frac{\partial q_{in}}{\partial \Delta P}\Delta P' = K_{reg}\Delta P'. \quad \text{(B3)}$$

As a result, Fig. 14 shows the linearized control system, the transform functions of which can be directly obtained as follows:

$$\begin{cases} \frac{P_b'(s)}{P_r'(s)} = \frac{K_\delta\left(K_{reg} + K_{seal}\right)}{s + K_\delta\left(K_{reg} + K_{seal}\right)}, \\ \frac{P_b'(s)}{P_c'(s)} = \frac{s}{s + K_\delta\left(K_{reg} + K_{seal}\right)}, \\ \frac{P_b'(s)}{\omega'(s)} = \frac{K_\omega s}{s + K_\delta\left(K_{reg} + K_{seal}\right)}. \end{cases} \quad \text{(B4)}$$

The system is stable according to the Routh-Hurwitz stability criterion. Furthermore, applying the final value theorem to the system leads to the following conclusions: (1) for a step input of P_r', the steady-state error between P_b' and P_r' is zero and (2) step inputs of P_r' and ω' would not change the steady-state value of P_b'. The conclusions are coincident with the experimental results in Fig. 9(c). Finally, the response time of the system can be reduced by increasing K_{reg} and K_{seal}. However, K_{seal} should be minimized to reduce water consumption. Therefore, the possible way to reduce the response time is to improve K_{reg} of the water pressure regulator.

APPENDIX C: THEORETICAL MODEL FOR RESISTING TORQUE

The red dashed line in Fig. 15 indicates the control volume. The output torque of the motor T_m is balanced with the resistance torque

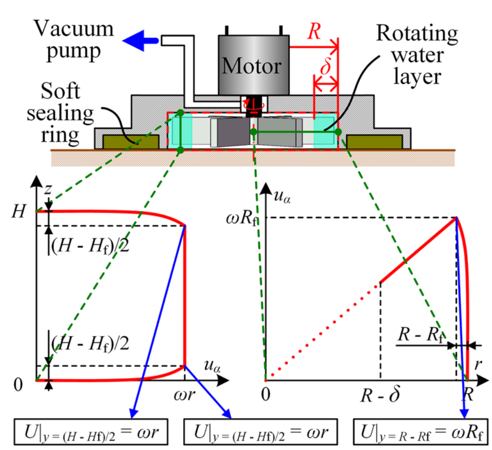

FIG. 15. Velocity distribution in the chamber.

of the control volume T_f, and the resistance torque can be obtained from the integral of the shear stress τ_w on the control surface,

$$T_m = T_f = \oiint_{S_0} \tau_w r\, ds. \tag{C1}$$

S_0 is the surface of the control volume, which consists of three parts: the upper wall of the chamber S_{upp}, cylindrical wall of the chamber S_{cyl}, and working surface S_{wor}. Accordingly, the resistance torque can be divided into three parts: T_{upp}, T_{cyl}, and T_{wor}. The shear stress τ_w on the surfaces is proportional to the velocity gradient on the wall,

$$\tau_w = \mu \left.\frac{\partial U}{\partial y}\right|_{y=0}, \tag{C2}$$

where μ is the dynamic viscosity of the fluid, y is the distance to the wall, and U is the velocity parallel to the wall as a function of y. The following friction velocity can be adopted:

$$U_\tau = \sqrt{\tau_w/\rho}. \tag{C3}$$

Then, y and U can be made dimensionless,

$$y^+ = \rho U_\tau y/\mu, \tag{C4}$$

$$U^+ = U/U_\tau. \tag{C5}$$

In the viscous layer ($y^+ < 5$), the velocity distribution can be described by[37,38]

$$U^+ = y^+ (y^+ < 5). \tag{C6}$$

In the turbulent layer ($y^+ > 20$), the velocity distribution for a hydraulically smooth wall follows the empirical 1/7th power law,[37,38]

$$U^+ = 8.74 y^{+1/7} (y^+ > 20). \tag{C7}$$

The region between viscous and turbulent layers is the buffer layer ($5 < y^+ < 20$). The fluid in the region swept by the fan is assumed to rotate like a rigid body (i.e., $u_\alpha = \omega r$), while the velocity in the region between the fan and walls is assumed to follow (C6) and (C7). Because $y = (H - H_f)/2$ should be located in the turbulent layer in practice, the shear stress on S_{upp} can be obtained by substituting the boundary condition $U|_{y=(H-Hf)/2} = \omega r$ into (C3),

$$\tau_w = \frac{0.0225\rho^{3/4}\mu^{1/4}\omega^{7/4}r^{7/4}}{[(H - H_f)/2]^{1/4}}. \tag{C8}$$

Because the air in the vacuum zone has much lower density and viscosity than water, the shear stress in $0 < r < R - \delta$ can be neglected. Therefore, T_{upp} can be obtained as

$$T_{upp} = \int_{R-\delta}^{R} 2\pi r^2 \tau_w dr = \frac{0.18\pi\rho^{3/4}\mu^{1/4}\omega^{7/4}\left[R^{19/4} - (R-\delta)^{19/4}\right]}{19[(H - H_f)/2]^{1/4}}. \tag{C9}$$

Similarly, T_{cyl} can be obtained by substituting $U|_{y=R-Rf} = \omega R_f$ into Eq. (C7) and integrating τ_w on S_{cyl},

$$T_{cyl} = \frac{0.045\pi\rho^{3/4}\mu^{1/4}\omega^{7/4}R_f^{7/4}R^2 H}{(R - R_f)^{1/4}}. \tag{C10}$$

When the working surface is smooth, T_{wor} can be calculated from the boundary condition $U|_{y=(H-Hf)/2} = \omega r$,

$$T_{wor} = \frac{0.18\pi\rho^{3/4}\mu^{1/4}\omega^{7/4}\left[R^{19/4} - (R-\delta)^{19/4}\right]}{19\left(\frac{H-H_f}{2}\right)^{1/4}}. \tag{C11}$$

When the working surface is rough, however, the following logarithmic wall function should be used instead,[37,38]

$$U^+ = \frac{1}{0.41}\ln\frac{y}{\varepsilon} + 8.5\left(\frac{\rho U_\tau \varepsilon}{\mu} > 70\right), \tag{C12}$$

where ϵ is the equivalent sand roughness. Consequently, T_{wor} is given by

$$T_{wor} = \frac{0.4\pi\rho\omega^2 R^5 - (R-\delta)^5}{\left(\frac{1}{0.41}\ln\frac{H-H_f}{2\varepsilon} + 8.5\right)^2}. \tag{C13}$$

Finally, the sum of T_{upp}, T_{cyl}, and T_{wor} is the output torque of the motor,

$$T_m = T_f = F_{upp} + F_{cyl} + T_{wor}. \tag{C14}$$

REFERENCES

[1] F. Tache, W. Fischer, G. Caprari, R. Siegwart, R. Moser, and F. Mondada, "Magnebike: A magnetic wheeled robot with high mobility for inspecting complex-shaped structures," J. Field Rob. **26**(5), 453–476 (2009).

[2] M. Tavakoli, C. Viegas, L. Marques, J. Norberto Pires, and A. T. de Almeida, "OmniClimbers: Omni-directional magnetic wheeled climbing robots for inspection of ferromagnetic structures," Rob. Auton. Syst. **61**(9), 997–1007 (2013).

[3] D. Roy, "Development of novel magnetic grippers for use in unstructured robotic workspace," Rob. Comput.-Integr. Manuf. **35**, 16–41 (2015).

[4] H. Wang and A. Yamamoto, "Analyses and solutions for the buckling of thin and flexible electrostatic inchworm climbing robots," IEEE Trans. Rob. **33**(4), 889–900 (2017).

[5] S. D. de Rivaz, B. Goldberg, N. Doshi, K. Jayaram, J. Zhou, and R. J. Wood, "Inverted and vertical climbing of a quadrupedal microrobot using electroadhesion," Sci. Rob. **3**(25), eaau3038 (2018).

[6] G. Gu, J. Zou, R. Zhao, X. Zhao, and X. Zhu, "Soft wall-climbing robots," Sci. Rob. **3**(25), eaat2874 (2018).

[7] K. Autumn, Y. A. Liang, S. T. Hsieh, W. Zesch, W. P. Chan, T. W. Kenny, R. Fearing, and R. J. Full, "Adhesive force of a single gecko foot-hair," Nature **405**(6787), 681–685 (2000).

[8] K. Autumn, A. Dittmore, D. Santos, M. Spenko, and M. Cutkosky, "Frictional adhesion: A new angle on gecko attachment," J. Exp. Biol. **209**(18), 3569–3579 (2006).

[9] S. Kim, M. Spenko, S. Trujillo, B. Heyneman, D. Santos, and M. R. Cutkosky, "Smooth vertical surface climbing with directional adhesion," IEEE Trans. Rob. **24**(1), 65–74 (2008).

[10] M. P. Murphy, C. Kute, Y. Menguec, and M. Sitti, "Waalbot II: Adhesion recovery and improved performance of a climbing robot using fibrillar adhesives," Int. J. Rob. Res. **30**(1), 118–133 (2011).

[11] W. Federle, M. Riehle, A. S. G. Curtis, and R. J. Full, "An integrative study of insect adhesion: Mechanics and wet adhesion of pretarsal pads in ants," Integr. Comp. Biol. **42**(6), 1100–1106 (2002).

[12] C. J. Clemente and W. Federle, "Pushing versus pulling: Division of labour between tarsal attachment pads in cockroaches," Proc. R. Soc. B **275**(1640), 1329–1336 (2008).

[13] Y. Wang, X. Yang, Y. Chen, D. K. Wainwright, C. P. Kenaley, Z. Gong, Z. Liu, H. Liu, J. Guan, T. Wang, J. C. Weaver, R. J. Wood, and L. Wen, "A biorobotic adhesive disc for underwater hitchhiking inspired by the remora suckerfish," Sci. Rob. **2**(10), eaan8072 (2017).

[14] R. Kolluru, K. P. Valavanis, A. Steward, and M. J. Sonnier, "A flat surface robotic gripper for handling limp material," IEEE Rob. Autom. Mag. **2**(3), 19–26 (1995).

[15] R. Kolluru, K. P. Valavanis, and T. M. Hebert, "Modeling, analysis, and performance evaluation of a robotic gripper system for limp material handling," IEEE Trans. Syst. Man Cybern. Part B-Cybern. **28**(3), 480–486 (1998).

[16] "Efficient robotic packing speeds soft drinks manufacture," Indus. Rob. **29**(3), 272–274 (2002).

[17] C. McKeown and P. Webb, "A reactive reconfigurable tool for aerospace structures," Assem. Autom. **31**(4), 334–343 (2011).
[18] S. Yu and M. Gil, "Manipulator handling device for assembly of large-size panels," Assem. Autom. **32**(4), 361–372 (2012).
[19] M. Monta, N. Kondo, and K. C. Ting, "End-effectors for tomato harvesting robot," Artif. Intell. Rev. **12**(1-3), 11–25 (1998).
[20] C. Blanes, V. Cortes, C. Ortiz, M. Mellado, and P. Talens, "Non-destructive assessment of mango firmness and ripeness using a robotic gripper," Food Bioprocess Technol. **8**(9), 1914–1924 (2015).
[21] K. Tanigaki, T. Fujiura, A. Akase, and J. Imagawa, "Cherry-harvesting robot," Comput. Electron. Agric. **63**(1), 65–72 (2008).
[22] P. Gan, "A novel liver retractor for reduced or single-port laparoscopic surgery," Surg. Endoscopy **28**(1), 331–335 (2014).
[23] P. Gan and J. Bingham, "A clinical study of the LiVac laparoscopic liver retractor system," Surg. Endoscopy **30**(2), 789–796 (2016).
[24] J. Kim, Y. Nakajima, and K. Kobayashi, "A suction-fixing, stiffness-tunable liver manipulator for laparoscopic surgeries," IEEE-ASME Trans. Mechatron. **23**(1), 262–273 (2018).
[25] J. A. Zhu, D. Sun, and S. K. Tso, "Application of a service climbing robot with motion planning and visual sensing," J. Rob. Syst. **20**(4), 189–199 (2003).
[26] H. X. Zhang, J. W. Zhang, and G. H. Zong, "Requirements of glass cleaning and development of climbing robot systems," in *Proceedings of the 2004 International Conference on Intelligent Mechatronics and Automation* (IEEE, 2004), pp. 101–106.
[27] Z.-Y. Qian, Y.-Z. Zhao, Z. Fu, and Q.-X. Cao, "Design and realization of a non-actuated glass-curtain wall-cleaning robot prototype with dual suction cups," Int. J. Adv. Manuf. Technol. **30**(1-2), 147–155 (2006).
[28] G. La Rosa, M. Messina, G. Muscato, and R. Sinatra, "A low-cost lightweight climbing robot for the inspection of vertical surfaces," Mechatronics **12**(1), 71–96 (2002).
[29] C. Balaguer, A. Gimenez, and M. Abderrahim, "ROMA robots for inspection of steel based infrastructures," Indus. Rob. **29**(3), 246–251 (2002).
[30] C. Hillenbrand, D. Schmidt, and K. Berns, "CROMSCI: Development of a climbing robot with negative pressure adhesion for inspections," Indus. Robot Int. J. **35**(3), 228–237 (2008).
[31] R. A. Kumar and G. Rajesh, "Flow transients in un-started and started modes of vacuum ejector operation," Phys. Fluids **28**(5), 056105 (2016).
[32] R. A. Kumar and G. Rajesh, "Physics of vacuum generation in zero-secondary flow ejectors," Phys. Fluids **30**(6), 066102 (2018).
[33] Y. Z. Zhao, Z. Fu, Q. X. Cao, and Y. Wang, "Development and applications of wall-climbing robots with a single suction cup," Robotica **22**, 643–648 (2004).
[34] D. Longo and G. Muscato, "The Alicia(3) climbing robot," IEEE Rob. Autom. Mag. **13**(1), 42–50 (2006).
[35] I. M. Koo, T. Tran Duc, Y. H. Lee, H. Moon, J. Koo, S. K. Park, and H. R. Choi, "Development of wall climbing robot system by using impeller type Adhesion mechanism," J. Intell. Rob. Syst. **72**(1), 57–72 (2013).
[36] X. Li and L. Dong, "Development and analysis of an electrically activated sucker for handling workpieces with rough and uneven surfaces," IEEE-ASME Trans. Mechatron. **21**(2), 1024–1034 (2016).
[37] X. Li and T. Kagawa, "Development of a new noncontact gripper using swirl vanes," Rob. Comput. Integr. Manuf. **29**(1), 63–70 (2013).
[38] X. Li, M. Horie, and T. Kagawa, "Pressure-distribution methods for estimating lifting force of a swirl gripper," IEEE-ASME Trans. Mechatron. **19**(2), 707–718 (2014).
[39] H. Schlichting, *Boundary-Layer Theory*, 6th ed. (McGraw-Hill, 1968).
[40] B. R. Munson, D. F. Young, T. H. Okiishi, and W. W. Huebsch, *Fundamentals of Fluid Mechanics*, 6th ed. (John Wiley & Sons, 2009).
[41] S. Raayai-Ardakani and G. H. McKinley, "Drag reduction using wrinkled surfaces in high Reynolds number laminar boundary layer flows," Phys. Fluids **29**(9), 093605 (2017).
[42] M. S. Naim and M. F. Baig, "Turbulent drag reduction in Taylor-Couette flows using different super-hydrophobic surface configurations," Phys. Fluids **31**(9), 095108 (2019).
[43] M. J. Spenko, G. C. Haynes, J. A. Saunders, M. R. Cutkosky, A. A. Rizzi, R. J. Full, and D. E. Koditschek, "Biologically inspired climbing with a hexapedal robot," J. Field Rob. **25**(4-5), 223–242 (2008).
[44] E. W. Hawkes, E. V. Eason, D. L. Christensen, and M. R. Cutkosky, "Human climbing with efficiently scaled gecko-inspired dry adhesives," J. R. Soc., Interface **12**(102), 20140675 (2015).